PHYSICAL REVIEW E **00**, 002300 (2019)

Diffusion dynamics of a conductance-based neuronal population

Argha Mondal,[1,2] Sanjeev Kumar Sharma,[1] Ranjit Kumar Upadhyay,[1] M. A. Aziz-Alaoui,[3] Prosenjit Kundu,[4] and Chittaranjan Hens[5,*]

[1]*Department of Applied Mathematics, Indian Institute of Technology (Indian School of Mines), Dhanbad 826004, India*
[2]*Computational Neuroscience Center, University of Washington, Seattle, Washington 98195, USA*
[3]*UniHavre, LMAH, CNRS No. 3335, ISCN, Normandie University, 76600 Le Havre, France*
[4]*National Institute of Technology Durgapur, Durgapur, West Bengal 713209, India*
[5]*Physics and Applied Mathematics Unit, Indian Statistical Institute, Barrackpore Trunk Road, Kolkata, West Bengal 700108, India*

(Received 9 October 2018; revised manuscript received 14 January 2019; published xxxxxx)

We study the spatiotemporal dynamics of a conductance-based neuronal cable. The processes of one-dimensional (1D) and 2D diffusion are considered for a single variable, which is the membrane voltage. A 2D Morris-Lecar (ML) model is introduced to investigate the nonlinear responses of an excitable conductance-based neuronal cable. We explore the parameter space of the uncoupled ML model and, based on the bifurcation diagram (as a function of stimulus current), we analyze the 1D diffusion dynamics in three regimes: phasic spiking, coexistence states (tonic spiking and phasic spiking exist together), and a quiescent state. We show (depending on parameters) that the diffusive system may generate regular and irregular bursting or spiking behavior. Further, we explore a 2D diffusion acting on the membrane voltage, where striped and hexagonlike patterns can be observed. To validate our numerical results and check the stability of the existing patterns generated by 2D diffusion, we use amplitude equations based on multiple-scale analysis. We incorporate 1D diffusion in an extended 3D version of the ML model, in which irregular bursting emerges for a certain diffusion strength. The generated patterns may have potential applications in nonlinear neuronal responses and signal transmission.

DOI: 10.1103/PhysRevE.00.002300

I. INTRODUCTION

Spatiotemporal pattern appears due to the occurrence of instability in a homogeneous medium sometimes referred to as Turing instability. The seminal work of Turing [1] led us to understand the emergence of stationary or nonstationary patterns in biological systems. He proposed that biological patterns (morphogenesis) arise due to the reaction and diffusion of chemicals in a homogeneous medium. This work has been further explored in many realistic situations ranging from evolution of patches in ecology [2–4] to pattern formation in chemical solutions [5]. Hair follicle [6], skin pigmentation [7,8], and tissue engineering mechanisms [9,10] and tomography of microemulsions [11] can also be related to diffusion-driven instability. The study of brain electrical dynamics suggests that one can understand the neurophysiological activities in the neural system by investigating the patterns emerging from the collective firing of a group of neurons. The mechanism of static spatial patterns or spatiotemporal neurological patterns can be understood in the light of the collective dynamics of neurons where they crosstalk with each other in a reaction-diffusion way [12]. Excitable media represent extended spatiotemporal systems that support wave propagation. Spiral breakup leading to turbulence can occur in a two-dimensional (2D) reaction-diffusion FitzHugh-Nagumo (FHN) system in which the spatial interaction is carried out only in membrane potential variables [13]. A two-component reaction-diffusion system of the FHN model was also investigated before the onset of subcritical Turing bifurcation [14]. Recently, Gambino *et al.* [15] constructed square and target wave patterns in a FHN reaction-diffusion system. The existence and stability of the patterns are derived with an amplitude equation analysis close to the bifurcation threshold. In the case of the bursting Hindmarsh-Rose model, the traveling-wave pattern was studied by Raghavachari and Glazier [16] for a 1D cable. In addition, the dynamics and synchronization pattern in the reaction-diffusion FHN system have been investigated by Ambrosio and Aziz-Alaoui [17]. The key question we raise here is whether an excitable cable in a conductance-based neuronal system can indeed generate bursting (regular or irregular) in the presence of 1D diffusion where the spatial interaction is carried out only in membrane potential variables. This is counterintuitive, as a homogeneous medium generates (through 1D diffusion) irregularity or instability without using the Turing-like diffusion structure. The 1D diffusion is a common scenario in many biophysical systems [18,19] in which one of the variables interacts with the others f in a spatially distributed cable. For instance, in excitable neuron models, the membrane voltage plays a major role as a diffusive variable in a spatial domain and influences the activities or firing patterns of the complete system. Moreover, in this type of situation no finite band of unstable wave numbers exists, therefore it violates the precondition of the Turing-type instability. In addition, we are exploring the processes in a 2D diffusion model of an excitable

*Corresponding author: chittaranjanhens@gmail.com

neural fiber. Various patterns ranging from regular hexagons to distorted hexagons are generated by the 2D diffusion in the conductance-based neuronal population. Further, we consider here an analytical treatment of a diffusive excitable cable to analyze the modulation and stability of structurally different patterns emerging from 2D diffusion.

We consider a 2D and a 3D version of a conductance-based Morris-Lecar (ML) oscillator [20] to describe the electrical activities of neurons. The ML models are taken into account because of their diverse complex behavior ranging from spiking to bursting nature mimicking the neuronal activities of neurons. A 2D ML oscillator is an excitable and reduced version of the Hodgkin-Huxley model. The model consists of voltage-gated calcium and delayed potassium conductances for excitatory and recovery processes. Then diffusively coupled ML neurons describe a network of neurons, i.e., the electrophysiology of excitable cables. We consider three regimes in the parameter space of the ML model: a phasic spiking (the neuron fires a single spike at the onset of the applied current stimulus and later it remains in a quiescent state) regime, a bistable regime where tonic spiking (oscillatory dynamics) and phasic spiking coexist together, and a regime wxhere the single neuron reaches a steady state [21,22]. We have shown that a systematic 1D diffusion acting on one variable (1D cable) may create spatial instability in the chain of oscillators. We examined the various impulses of the 1D cables. It has already been established that the analysis for spatial mechanisms and its activity for neuronal cells is important to understand the biophysical and pathological activities [23–25]. Mainly, we try to find a region in the parameter space in which a bursting regime can emerge from a single cell when the cells are connected by 1D diffusive coupling to an extended continuous reaction-diffusion medium. Note that, while bursting of a single neuron is physiological, bursting of a fundamental cell consisting of a network of neurons is potentially pathological [12]. Our investigation shows that the system reveals a burstinglike nature at the lower diffusion, although the uncoupled system stays in the phasic spiking regime or in coexisting states (phasic spiking and tonic spiking). If we increase the diffusion coefficient, the network returns to the homogeneous steady states. Further, we have incorporated a 2D diffusion (2D cable) and observed that the system may show a complex pattern ranging from stable (unstable) hexagons to unstable stripes. We have analytically derived the emergence and stability of these patterns and successfully verified with numerical results. Interestingly, the possible patterns for 2D diffusion show complex behavior and this emergent dynamics may have relevance in the synchronized activities of a population of neurons particularly for neurological diseases [12]. The propagation of neuronal impulses in the coupled network is very relevant for brain functioning [26–28]. However, a clear and concise analytical treatment describing different collective nonlinear responses of the diffusively coupled ML neurons in three different regimes is lacking. We have used multiple-scale analysis [3,29–31] for 2D pattern selection based on the amplitude equations introduced by Newell and Whitehead [32] and Segel [33].

Further, the model of a single neuron is extended to its 3D counterpart, in which the applied current stimulus is not constant but rather changes in time. The uncoupled slow-fast model produces regular bursting for a fixed set of parameters whereas the coupled 1D chain generates irregular bursting, which is an interesting feature in biophysical systems.

The paper is organized as follows. In Sec. II the uncoupled 2D ML model is described. In Sec. III the impact of 1D diffusion is examined for different diffusion strengths. The proper parameter space of bursting is identified. Other firing activities and instabilities are demonstrated. Further, the complex patterns emerging for 2D diffusion are discussed in Sec. IV with amplitude equations. We study the 1D cable in an extended 3D version of ML model in Sec. V. Section VI provides a summary and conclusions.

II. FORMULATION AND DYNAMICS OF 2D ML NEURONS

Morris and Lecar [20,34] suggested a simple mathematical model to describe the oscillations in barnacle giant muscle fiber. It consists of a membrane potential equation with instantaneous activation of calcium current and an additional equation describing slower activation of potassium current. The ML neuron model is described by

$$\begin{aligned} C\dot{u} &= I - g_L(u - V_L) - g_{\mathrm{Ca}} m_\infty (u - V_{\mathrm{Ca}}) - g_{\mathrm{K}} v (u - V_{\mathrm{K}}), \\ \dot{v} &= \lambda(u)[v_\infty(u) - v], \end{aligned} \tag{1}$$

where m_∞, v_∞, and $\lambda(u)$ are assumed as the functions $m_\infty = 0.5\{1 + \tanh[(u - V_1)/V_2]\}$, $v_\infty = 0.5\{1 + \tanh[(u - V_3)/V_4]\}$, and $\lambda(u) = \phi \cosh[(u - V_3)/2V_4]$, respectively.

The system consists of voltage-gated Ca^{2+} current, delayed rectifier K^+ current, and the leak current, respectively. Here u represents the membrane potential of the neuron and v is the activation variable of K^+ ion channels. The parameters g_{Ca}, g_{K}, and g_L indicate the maximum conductance functions to Ca^{2+}, K^+, and leak currents, respectively, and V_{Ca}, V_{K}, and V_L are the reversal potentials to the different ionic current functions. Further, C measures the membrane capacitance and it is considered as unity; ϕ represents the temperature scaling factor for the K^+ channel opening. The parameters V_1 and V_3 measure the potential at which $m_\infty = 0.5$ and $v_\infty = 0.5$, respectively, and V_3 and V_4 represent the reciprocal slope of the voltage dependence of m_∞ and v_∞, respectively. In addition, I presents the applied stimulus current [20,21]. We would like to consider the effects of various injected current stimuli for the deterministic 2D ML model, which shows phasic spiking, tonic spiking, and fast spiking.

To study the characteristic description of the ML model for different sets of current stimuli, we linearly perturb the system around the fixed point (u^*, v^*). The Jacobian matrix corresponding to the equilibrium is

$$J = \begin{pmatrix} a_{11} & a_{12} \\ a_{21} & a_{22} \end{pmatrix}, \tag{2}$$

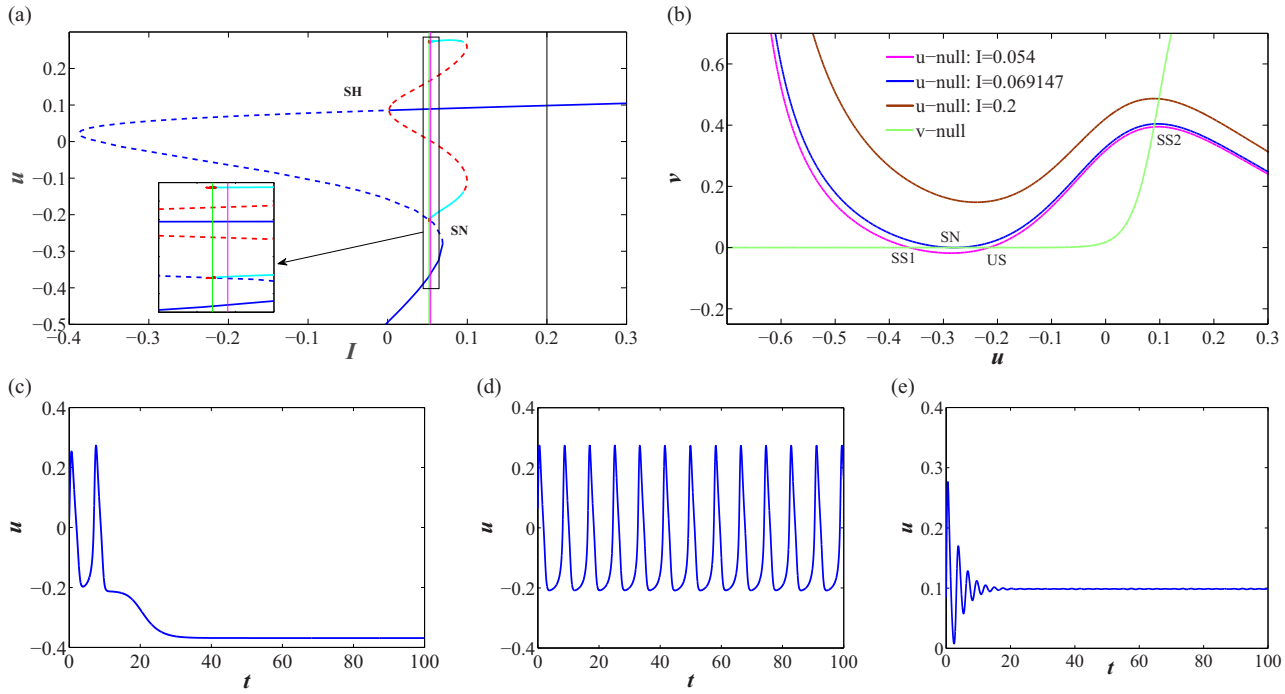

FIG. 1. (a) Bifurcation diagram of the 2D ML oscillator with respect to the stimulus current I. The thick solid blue line indicates the stable equilibrium branch whereas the dotted blue line indicates the unstable equilibrium branch of the system. The stable and unstable limit cycles are denoted by solid cyan and dotted red lines, respectively. Points SH and SN represent the subcritical Hopf bifurcation and saddle-node bifurcation, respectively. (b) Nullclines are plotted for the deterministic uncoupled 2D ML model. The intersections of the u nullcline and v nullcline are the fixed points: the stable steady states (SS1 and SS2), unstable steady state (US), and saddle-node bifurcation (SN). The time series of the deterministic uncoupled 2D ML model for different regimes [marked by the vertical lines in (a)] of I are (c) $I = 0.052$ [vertical green line in the inset of (a)], (d) $I = 0.054$ [vertical magenta line in the inset of (a)], and (e) $I = 0.2$ (vertical black line), respectively.

where

$$a_{11} = -0.5g_{\mathrm{Ca}}\left[1+\tanh\left(\frac{u^*-V_1}{V_2}\right)+\left(\frac{u^*-1}{V_2}\right)\mathrm{sech}^2\left(\frac{u^*-V_1}{V_2}\right)\right]\Big/C-\frac{g_{\mathrm{K}}v^*}{C}-\frac{g_L}{C},\quad a_{12}=\frac{1}{C}[-g_{\mathrm{K}}(u^*-V_{\mathrm{K}})],$$

$$a_{21} = \left(\frac{\phi}{2V_4}\right)\left\{0.5\left[1+\tanh\left(\frac{u^*-V_3}{V_4}\right)\right]-v^*\right\}\sinh\left(\frac{u^*-V_3}{2V_4}\right)+x\left(\frac{\phi}{V_4}\right)\cosh\left(\frac{u^*-V_3}{2V_4}\right)0.5\,\mathrm{sech}^2\left(\frac{u^*-V_3}{V_4}\right),$$

$$a_{22} = \left(-\frac{1}{3}\right)\cosh\left(\frac{u^*-V_3}{2V_4}\right).$$

The condition for the equilibrium solution of the system to be stable for the deterministic model is given by $a_{11}+a_{22}<0$ and $a_{11}a_{22}-a_{12}a_{21}>0$. The stability analysis of the above ML model is discussed for the following parameter values [21]: $C=1$, $g_L=0.5$, $V_L=-0.5$, $g_{\mathrm{Ca}}=1.2$, $V_{\mathrm{Ca}}=1$, $g_{\mathrm{K}}=2$, $V_{\mathrm{K}}=-0.7$, $V_1=-0.01$, $V_2=0.15$, $V_3=0.1$, $V_4=0.05$, and $\phi=1/3$.

The bifurcation analysis for the 2D ML system is derived using MATCONT software by varying the injected current stimulus I. At higher injected current stimulus ($I>0.1$), the model reveals a monostable quiescent state (stable focus). The unstable state becomes stable as a result of the subcritical Hopf bifurcation (SH) at lower positive value of stimulus current ($I\sim 0.001\,830$). In Fig. 1(a), the upper thick blue line describes the changes of this quiescent state for different sets of stimulus current. The lower thick blue line describes a stable node which collides with a saddle point at $I\sim 0.069\,147$ [SN point in Fig. 1(a)] and vanishes together. We use phase-space analysis to understand the behavior of the existing fixed points. The deterministic system has three equilibrium points that are the intersections of the nullclines of the system variables u and v, respectively. The left fixed point (SS1) is asymptotically stable (stable node) and right fixed point (US) is unstable [see Fig. 1(b)]. When the current stimulus I is increased, the u nullcline moves upward and the two fixed points move closer to each other, collide, and mutually annihilate, resulting in a saddle node bifurcation (SN). After that there exists only one fixed point (SS2) with a further increase of I. There is another interesting behavior appearing between $I\sim 0.053$ and $I\sim 0.99$. A stable limit cycle (thick cyan line) coexists with an unstable limit cycle shown by the dashed red line (also see the inset). Therefore, the system becomes tristable, i.e., one stable node, one limit cycle, and one stable focus coexist together. The thick green

lines and dotted red lines show stable and unstable limit cycles, respectively. This type of feature arises due to the impact of hyperbolic functions in the ML system. For our analysis, we consider three parameter spaces. The system produces phasic spiking at $I = 0.052$; the value is marked in the figure with vertical green line in extreme left [Fig. 1(a), also in the inset]. The corresponding time series for phasic spiking is shown in Fig. 1(c). A limit cycle (tonic spiking) is produced at $I = 0.054$; the value is marked with middle vertical magenta line in Fig. 1(a) and the corresponding time series is shown in Fig. 1(d). The quiescent state at $I = 0.2$ is marked by the rightmost vertical solid black line in Fig. 1(a) and corresponding time series is shown in Fig. 1(e).

III. ONE-DIMENSIONAL SYSTEM OF 2D ML NEURONS WITH DIFFUSION COUPLING

We investigate a 1D cable consisting of a chain of excitable neurons. A nearest-neighbor diffusion through the membrane potential (variable u) is considered in our study. The 2D excitable ML model with 1D diffusion is described by the reaction-diffusion equations

$$\begin{aligned} C\frac{\partial u}{\partial t} &= I - g_L(u - V_L) - g_{\mathrm{Ca}} m_\infty (u - V_{\mathrm{Ca}}) \\ &\quad - g_{\mathrm{K}} v(u - V_{\mathrm{K}}) + D\frac{\partial^2 u}{\partial x^2}, \\ \frac{\partial v}{\partial t} &= \lambda(u)[v_\infty(u) - v]. \end{aligned} \tag{3}$$

The initial conditions of these partial differential equations (PDEs) are considered as $u(t = 0, x) > 0$ and $v(t = 0, x) > 0$ for $x \in \Psi$ and the boundary conditions are zero-flux boundary conditions $\frac{\partial u}{\partial n} = \frac{\partial v}{\partial n} = 0$ for $x \in \partial\Psi$ and $t > 0$, where n is the outward normal to $\partial\Psi$, the boundary of the interval and domain, and Ψ is the bounded interval or square domain for 1D and 2D diffusion. In the 1D case, it is the length of the excitable cable ($N = 10$) and D is the strength of the synaptic coupling. We use a finite-difference scheme for numerical simulation of a cable of finite length. The numerical solution for the 1D reaction-diffusion system is computed using the `pdepe` method with zero-flux boundary conditions. The time step $\Delta t = 0.001$ and space step $\Delta x = 0.1$ are considered and are fixed for all the 1D simulations. The zero-flux boundary condition indicates that the membranes are impermeable at the boundaries and it acts as an isolated cable [12].

We apply an external stimulus I to all the excitable neurons. As we have mentioned before, this external stimulus can change the dynamical behavior of the uncoupled model. We have investigated the spatiotemporal pattern in three regimes, observed at different values of I. First, the impact of the diffusion coefficient D has been tested by setting each neuron in a phasic spiking state ($I = 0.052$), i.e., all the neurons are settled into the phasic spiking regime [Fig. 1(c)]. At a lower diffusion ($D = 0.0001$), the system loses its stability and creates a nonhomogeneous irregular pattern [Fig. 2(a)], corresponding to a spiral-type instability. The vertical yellow and blue strips signify small oscillations deviated from the original uncoupled steady states. For a better understanding, we show the time series for an arbitrarily chosen node in Fig. 3(a). Here there is spatial heterogeneity, but if we consider an oscillatory node (vertical yellow strips) from the cable it shows oscillations. At a higher diffusion ($D = 0.0005$ and $D = 0.0037$), a more complex desynchronized firing pattern [Figs. 2(b) and 2(c)] appears where a train of irregular spiking and bursting [Figs. 3(b) and 3(c)] is generated. Finally, the spatial instability has vanished for a higher diffusion coefficient ($D = 0.5$) by stabilizing the whole chain or cable into a homogeneous fixed point [see Figs. 2(d) and 3(d)], which is the stable node of an uncoupled neuron. We observe how firing patterns of a neuronal cable can change by the impact of the diffusion coefficient value D. With systematic changes in the value of D, the continuous medium (cable) passes from the regime of inhomogeneous instability to a uniform steady state [35] through the formation of irregular structures at intermediate values of diffusion coefficients. Next we consider a slightly increased external current ($I = 0.054$). For this parameter value, regular periodic oscillations like bursting emerge at an intermediate diffusion value. The initial emergence of instability, an irregular spiking pattern, periodic or regular bursting, and collective quiescent states has been tested for the same diffusion coefficients ($D = 0.0001$, 0.0005, 0.0037, and 0.5, respectively). The spatiotemporal patterns are shown in Figs. 2(e)–2(h) and the corresponding time series are shown in Figs. 3(e)–3(h). Note that, in a weakly coupled network of pancreatic β cells, the bursting behavior becomes predominant in which pancreatic β cell secretes insulin in the blood [16,36]. As we have discussed before, each neuron has tristable behavior in this regime: Two of them are stable fixed points (stable focus and stable node) and the other is a limit cycle (tonic spiking). The basin of attraction (not shown here) for each of those states is well mixed in the coupled network, creating a periodic bursting-type nature at an intermediate coupling strength analogous to the periodic bursting pattern emerging in globally coupled discretized active-inactive Josephson junctions [37]. Next we consider each unit in a monostable quiescent state ($I = 0.2$), a state far away from the bifurcation point (SH). At lower diffusion, the system shows instability that creates an irregular firing pattern [Fig. 2(i)]. Surprisingly, few nodes fire aperiodically with high amplitudes [Fig. 3(i)], although a small increase in the diffusion strength returns the continuous cable to the original quiescent state shown in Figs. 2(j)–2(l) and 3(j)–3(l).

IV. TWO-DIMENSIONAL SYSTEM OF 2D ML NEURONS WITH DIFFUSION COUPLING

Now we extend our study of spatiotemporal patterns by allowing 2D diffusion only in the membrane potential variable in the excitable 2D ML system (1). The system is described by the PDEs

$$\begin{aligned} C\frac{\partial u}{\partial t} &= I - g_L(u - V_L) - g_{\mathrm{Ca}} m_\infty (u - V_{\mathrm{Ca}}) \\ &\quad - g_{\mathrm{K}} v(u - V_{\mathrm{K}}) + D\left(\frac{\partial^2 u}{\partial x^2} + \frac{\partial^2 u}{\partial y^2}\right), \\ \frac{\partial v}{\partial t} &= \lambda(u)[v_\infty(u) - v], \end{aligned} \tag{4}$$

with the same initial and boundary conditions as before.

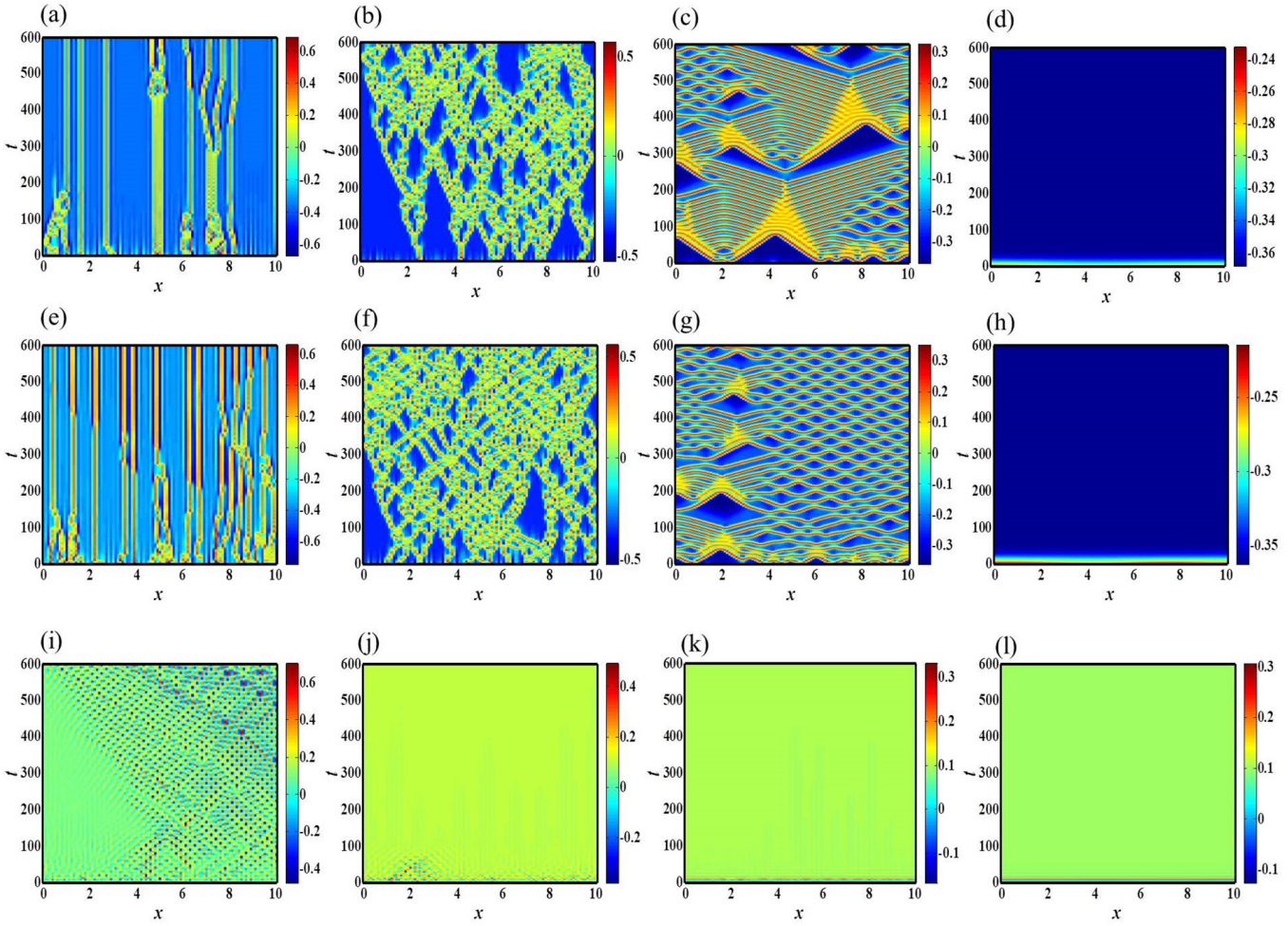

FIG. 2. Spatiotemporal plots of the 2D ML cable with 1D diffusion for (a)–(d) $I = 0.052$, (e)–(h) $I = 0.054$, and (i)–(l) $I = 0.2$ and diffusion coefficients (a), (e), and (i) $D = 0.0001$; (b), (f), and (j) $D = 0.0005$; (c), (g), and (k) $D = 0.0037$; and (d), (h), and (l) $D = 0.5$. The color bar of all these spatiotemporal plots indicates the value of the membrane voltage u. Transient parts are also shown to understand the patterns clearly.

A. Amplitude equations

We have applied the multiple-scale analysis method [3,29,38,39] near the bifurcation point. The relevant patterns can be expressed by three active resonant pairs of modes $(k_j, -k_j)$ such that $|k_j| = k_T$ for $j = 1, 2, 3$. Expanding the two trigonometric hyperbolic functions present in the system and avoiding the higher-order nonlinear terms, we reach $\tanh(x) \sim x - \frac{x^3}{3}$ and $\cosh(x) \sim 1 + \frac{x^2}{2!}$. Inserting these expressions into Eq. (1), we get

$$\dot{u} = I - g_L(u - V_L) - 0.5 g_{\mathrm{Ca}}(u - V_{\mathrm{Ca}}) \times \left[1 + \frac{u - V_1}{V_2} - \frac{(u - V_1)^3}{3V_2{}^3}\right] - g_{\mathrm{K}} v (u - V_{\mathrm{K}}), \quad (5)$$

$$\dot{v} = \frac{0.5}{3}\left[1 + \frac{(u - V_3)^2}{8V_4^2}\right] \times \left[1 + \frac{u - V_3}{V_4} - \frac{(u - V_3)^3}{3V_4^3} - \frac{v}{0.5}\right], \quad (6)$$

where the meaning of the parameters V_1, V_2, V_3, and V_4 is the same as mentioned in Sec. II. Now simplifying the above system, we obtain

$$\dot{u} = I + a_1 u + a_2 v + a_3 u^2 + a_4 uv + a_5 u^3 + a_6, \quad (7)$$

$$\dot{v} = b_1 u + b_2 v + b_3 u^2 + b_4 uv + b_5 u^3 + b_6 u^2 v + b_7. \quad (8)$$

The expressions for all the coefficients of the above equations are given in Appendix B. We consider a small perturbation $u = \tilde{u} + u^*$ and $v = \tilde{v} + v^*$ around the equilibrium point (u^*, v^*). Then, expanding it with in a Taylor series expansion and truncating the expression up to third order, we obtain

$$\frac{\partial \tilde{u}}{\partial t} = a_{11}\tilde{u} + a_{12}\tilde{v} + (a_3 + 3a_5 u^*)\tilde{u}^2 + a_4 \tilde{u}\tilde{v} + a_5 \tilde{u}^3 + D\nabla^2 \tilde{u}, \quad (9)$$

$$\frac{\partial \tilde{v}}{\partial t} = a_{21}\tilde{u} + a_{22}\tilde{v} + (b_3 + 3b_5 u^* + b_6 v^*)\tilde{u}^2 + (b_4 + 2b_6 u^*)\tilde{u}\tilde{v} + b_5 \tilde{u}^3 + b_6 \tilde{u}^2 \tilde{v}. \quad (10)$$

Equations (9) and (10) can be written in the vector form

$$\frac{\partial X}{\partial t} = LX + H, \quad (11)$$

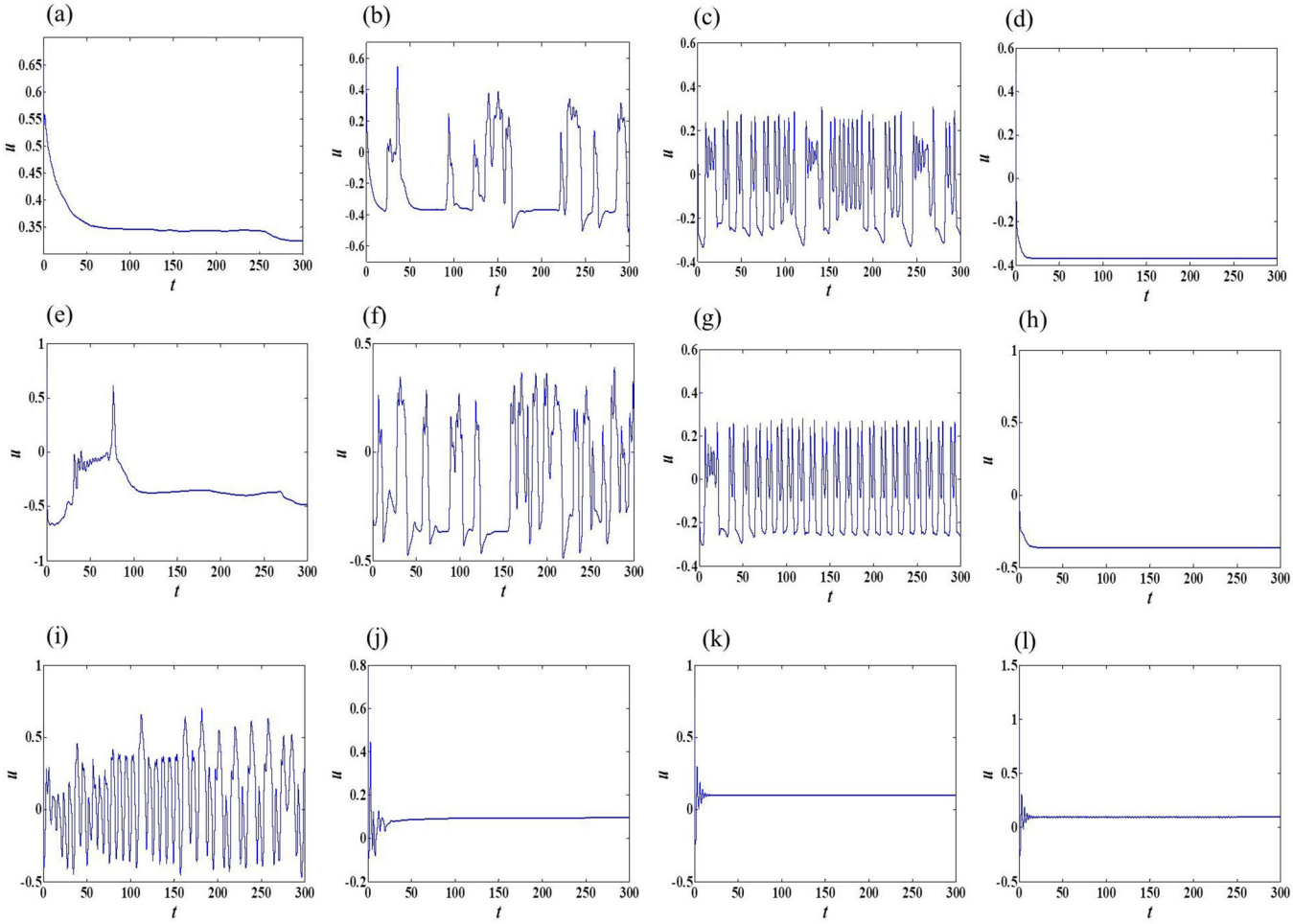

FIG. 3. Time series of the end oscillator of the 2D ML cable with 1D diffusion. The external current stimulus is (a)–(d) $I = 0.052$, (e)–(h) $I = 0.054$, and (i)–(l) $I = 0.2$. The values of the diffusion coefficients for all the panels are the same as in Fig. 2. We choose the end oscillator as a random node to show the temporal evaluation for each panel.

where

$$X = \begin{pmatrix} \tilde{u} \\ \tilde{v} \end{pmatrix}, \quad L = \begin{pmatrix} a_{11} + D\nabla^2 & a_{12} \\ a_{21} & a_{22} \end{pmatrix},$$

$$H = [(a_3 + 3a_5u^*)\tilde{u}^2 + a_4\tilde{u}\tilde{v} + a_5\tilde{u}^3(b_3 + 3b_5u^* + b_6v^*)\tilde{u}^2 + (b_4 + 2b_6u^*)\tilde{u}\tilde{v} + b_5\tilde{u}^3 + b_6\tilde{u}^2\tilde{v}].$$

We expand the bifurcation parameter I as $I - I_T = \varepsilon I_1 + \varepsilon^2 I_2 + \varepsilon^3 I_3 + o(\varepsilon^3)$, where $|\varepsilon| \ll 1$ and I_T is the Hopf bifurcation point. Similarly, we expand the variable X and the nonlinear term H,

$$X = \begin{pmatrix} \tilde{u} \\ \tilde{v} \end{pmatrix} = \varepsilon \begin{pmatrix} p_1 \\ q_1 \end{pmatrix} + \varepsilon^2 \begin{pmatrix} p_2 \\ q_2 \end{pmatrix} + \varepsilon^3 \begin{pmatrix} p_3 \\ q_3 \end{pmatrix} + o(\varepsilon^3) \quad (12)$$

and

$$H = \varepsilon^2 h_2 + \varepsilon^3 h_3 + o(\varepsilon^3), \quad (13)$$

where h_2 and h_3 are the second and third orders of ε in the expansion of the nonlinear term H. At the same time, the linear operator L can be written as

$$L = L_T + (I - I_T)L_1 + (I - I_T)^2 L_2 + o((I - I_T)^3), \quad (14)$$

$$L = L_T + (I - I_T)M + o((I - I_T)^2), \quad (15)$$

where

$$L_i = \frac{1}{i!}\frac{\partial^i L}{\partial I^i},$$

$$L_T = \begin{pmatrix} a_{11}^T + D\nabla^2 & a_{12}^T \\ a_{21}^T & a_{22}^T \end{pmatrix},$$

$$M = \begin{pmatrix} m_{11} & m_{12} \\ m_{21} & m_{22} \end{pmatrix}.$$

Now we can split the typical timescale in the time derivative by [4]

$$\frac{\partial}{\partial t} = \varepsilon \frac{\partial}{\partial T_1} + \varepsilon^2 \frac{\partial}{\partial T_2} + o(\varepsilon^2), \quad (16)$$

where $T_1 = \varepsilon t$ and $T_2 = \varepsilon^2 t$.

We have, from Eq. (11),

$$\frac{\partial}{\partial t}\left\{\varepsilon\begin{pmatrix}p_1\\q_1\end{pmatrix}+\varepsilon^2\begin{pmatrix}p_2\\q_2\end{pmatrix}+\varepsilon^3\begin{pmatrix}p_3\\q_3\end{pmatrix}\right\} = \{L_T+(I-I_T)M\}X+\varepsilon^2 h_2+\varepsilon^3 h_3.$$

Simplifying the above equation and comparing the order of ε, ε^2, and ε^3 from both sides, we obtain

$$L_T\begin{pmatrix}p_1\\q_1\end{pmatrix}=0, \tag{17}$$

$$L_T\begin{pmatrix}p_2\\q_2\end{pmatrix}=\frac{\partial}{\partial T_1}\begin{pmatrix}p_1\\q_1\end{pmatrix}-I_1M\begin{pmatrix}p_1\\q_1\end{pmatrix}-h_2, \tag{18}$$

$$L_T\begin{pmatrix}p_3\\q_3\end{pmatrix}=\frac{\partial}{\partial T_1}\begin{pmatrix}p_2\\q_2\end{pmatrix}+\frac{\partial}{\partial T_2}\begin{pmatrix}p_1\\q_1\end{pmatrix}-I_1\times M\begin{pmatrix}p_2\\q_2\end{pmatrix}-I_2M\begin{pmatrix}p_1\\q_1\end{pmatrix}-h_3. \tag{19}$$

The expressions of h_2 and h_3 are described in Appendix B. Solving Eq. (17), we get $p_1=\frac{a_{12}^T}{Dk^2-a_{11}^T}=f$ and $q_1=1$ and we can write

$$\begin{pmatrix}p_1\\q_1\end{pmatrix}=\begin{pmatrix}f\\1\end{pmatrix}\left(\sum_{j=1}^{3}W_j\exp(ik_jr)+\text{c.c.}\right), \tag{20}$$

i.e., (p_1, q_1) is the linear combination of the eigenvectors that corresponds to the zero eigenvalue of the linear operation L_T, where W_j is the amplitude of the mode $\exp(ik_jr)$ and c.c. represents complex conjugate. Now, to get the nontrivial solution of Eq. (18), we use the Fredholm solvability criterion [3], where the zero eigenvectors of operator $L_T^\dagger$ (the adjoint operator of L_T) must be orthogonal to the right-hand side of Eq. (18). Note that the zero eigenvectors of the operator $L_T^\dagger$ are described as $\binom{1}{g}[\exp(-ik_jr)+\text{c.c.}]$, $j=1,2,3$, where $g=-\frac{a_{12}^T}{a_{22}^T}$. Now, from Eq. (18) we can write

$$L_T\begin{pmatrix}p_2\\q_2\end{pmatrix}\triangleq\begin{pmatrix}F_p\\F_q\end{pmatrix}.$$

Here F_p^j and F_q^j represent the coefficients of $\exp(ik_jr)$ in F_p and F_q, respectively. Using the orthogonality condition $(1,g)\binom{F_p^j}{F_q^j}=0$, we can reach the relations

$$\begin{aligned}(f+g)\frac{\partial W_1}{\partial T_1}&=I_1[fm_{11}+m_{12}+g(fm_{21}+m_{22})]W_1\\&\quad+2(l_1+gl_2)\bar{W}_2\bar{W}_3,\\(f+g)\frac{\partial W_2}{\partial T_1}&=I_1[fm_{11}+m_{12}+g(fm_{21}+m_{22})]W_2\\&\quad+2(l_1+gl_2)\bar{W}_1\bar{W}_3,\\(f+g)\frac{\partial W_3}{\partial T_1}&=I_1[fm_{11}+m_{12}+g(fm_{21}+m_{22})]W_3\\&\quad+2(l_1+gl_2)\bar{W}_1\bar{W}_2.\end{aligned}$$

Solving Eq. (18), we have

$$\begin{aligned}\begin{pmatrix}p_2\\q_2\end{pmatrix}&=\begin{pmatrix}P_0\\Q_0\end{pmatrix}+\sum_{j=1}^{3}\begin{pmatrix}P_j\\Q_j\end{pmatrix}\exp(ik_jr)\\&\quad+\sum_{j=1}^{3}\begin{pmatrix}P_{jj}\\Q_{jj}\end{pmatrix}\exp(i2k_jr)\\&\quad+\begin{pmatrix}P_{12}\\Q_{12}\end{pmatrix}\exp[i(k_1-k_2)r]+\begin{pmatrix}P_{23}\\Q_{23}\end{pmatrix}\exp[i(k_2-k_3)r]\\&\quad+\begin{pmatrix}P_{31}\\Q_{31}\end{pmatrix}\exp[i(k_3-k_1)r]+\text{c.c.}\end{aligned} \tag{21}$$

The coefficients of Eq. (21) are described in Appendix B. Using the approach described above and following the Fredholm solvability criterion, we get [from Eq. (19)]

$$\begin{aligned}(f+g)&\left(\frac{\partial W_1}{\partial T_2}+\frac{\partial Q_1}{\partial T_1}\right)\\&=[fm_{11}+m_{12}+g(fm_{21}+m_{22})]\\&\quad\times(I_1Q_1+I_2W_1)+\mathbf{H}(\bar{Q}_2\bar{W}_3+\bar{Q}_3\bar{W}_2)\\&\quad-[G_1|W_1|^2+G_2(|W_2|^2+|W_3|^2)]W_1.\end{aligned} \tag{22}$$

The remaining two equations (not shown here) can be obtained through the transformation of the subscripts of W and Q. Here A_j and its conjugate $\bar{A}_j$ $(j=1,2,3)$ are the amplitudes of the modes k_j and $-k_j$, respectively. The amplitude A_j can be expanded as $A_j=\varepsilon W_j+\varepsilon^2Q_j+o(\varepsilon^3)$. With the expression of A_j and Eq. (16), we can obtain the amplitude equation corresponding to A_1 as

$$\begin{aligned}\tau_0\frac{\partial A_1}{\partial t}&=\mu A_1+h\bar{A}_2\bar{A}_3-[g_1|A_1|^2\\&\quad+g_2(|A_2|^2+|A_3|^2)]A_1,\end{aligned} \tag{23}$$

where $\mu=(I-I_T)/I_T$ is a normalized distance to the onset and g_1 and g_2 explore the type of instability [40]. Expressions for the factors g_1, g_2, τ_0, and h are given in Appendix B. In the same way, we can calculate the remaining two equations (evaluation of A_2 and A_3).

B. Amplitude stability

We can transform the amplitude equations [Eq. (23) for A_2 and A_3] from rectangular coordinates to polar coordinates by setting the complex amplitude as $A_j=\rho_j\exp(i\varphi_j)$, where $\rho_j=|A_j|$ and φ_j represents the phase angle in the system. Finally, we get a set of coupled equations with a constraint $(\varphi=\varphi_1+\varphi_2+\varphi_3)$

$$\begin{aligned}\tau_0\frac{\partial\varphi}{\partial t}&=-h\frac{\rho_1^2\rho_2^2+\rho_1^2\rho_3^2+\rho_2^2\rho_3^2}{\rho_1\rho_2\rho_3}\sin\varphi,\\\tau_0\frac{\partial\rho_1}{\partial t}&=\mu\rho_1+h\rho_2\rho_3\cos\varphi-g_1\rho_1^3-g_2\left(\rho_2^2+\rho_3^2\right)\rho_1,\\\tau_0\frac{\partial\rho_2}{\partial t}&=\mu\rho_2+h\rho_1\rho_3\cos\varphi-g_1\rho_2^3-g_2\left(\rho_1^2+\rho_3^2\right)\rho_2,\\\tau_0\frac{\partial\rho_3}{\partial t}&=\mu\rho_3+h\rho_1\rho_2\cos\varphi-g_1\rho_3^3-g_2\left(\rho_1^2+\rho_2^2\right)\rho_3.\end{aligned} \tag{24}$$

Depending on the parameters μ, g_1, g_2, and h, the 2D cable can reveal structurally different patterns including stationary, striped, and hexagons. (i) The stationary state is given by

$$\rho_1 = \rho_2 = \rho_3 = 0$$

and is stable for $\mu < \mu_2 = 0$ and unstable for $\mu > \mu_2$. (ii) The striped pattern is given by

$$\rho_1 = \sqrt{\frac{\mu}{g_1}} \neq 0, \quad \rho_2 = \rho_3 = 0$$

and the stable striped pattern occurs when $\mu > \mu_3 = \frac{h^2 g_1}{(g_2 - g_1)^2}$ and it becomes unstable for $\mu < \mu_3$. (iii) The hexagonal patterns exist when

$$\rho_1 = \rho_2 = \rho_3 = \frac{|h| \pm \sqrt{h^2 + 4(g_1 + 2g_2)\mu}}{2(g_1 + 2g_2)},$$

with $\varphi = 0$ or π and when $\mu > \mu_1 = \frac{-h^2}{4(g_1+2g_2)}$.

The hexagonal pattern H_π (when $\varphi = \pi$) will be stable only for $\mu < \mu_4 = \frac{2g_1+g_2}{(g_2-g_1)^2}h^2$ and H_0 (when $\varphi = 0$) is always unstable. For detailed calculation and identification of the parameters see Appendix A. We consider the same ML model explored for 1D diffusion as described in Sec. III. With the fixed set of parameters $I = 0.052$ and $D = 0.001$, we obtain $h = 4075.55$, $g_1 = -17\,95\,960$, $g_2 = -2\,388\,310$, $\mu_1 = 0.631\,794$, $\mu_2 = 0$, $\mu_3 = -85.0156$, $\mu_4 = -283.087$, and $\mu^* = 27.4153$. Here positive h indicates that there exist H_0 hexagons as $\mu^* > \mu_1$ and striped patterns do not exist (as $\rho_1 = \sqrt{\frac{\mu^*}{g_1}}$ becomes imaginary). As H_0 is always unstable, the solutions of ρ [Eq. (24)] will not exist. The existence of H_0 (although unstable) throughout a long range of diffusion coefficient D is shown in Fig. 4(a), where it is clear that μ^* (dashed magenta line) is always greater than μ_1 (existence condition shown by the solid black line). As a result, we observe a mixture of regular and distorted hexagons (on a blue backdrop), shown in the Fig. 5(a) (also a zoomed-in view of the regular hexagons is marked with a white dashed rectangle). However, as we increase the value of the diffusion coefficient D we observe distorted hexagons [Figs. 5(b) and 5(c)] only. Interestingly, if we increase D, it creates less amplitude fluctuation in the membrane voltage expecting a homogeneous pattern at higher D. Note that one can solve the amplitude equations for negative $g_{1,2}$ by considering the higher-order approximations to get a better stability condition [40] for hexagonal patterns, which is beyond the scope of the present work.

Similarly, for $I = 0.054$ and $D = 0.001$, we obtain $h = 11\,372$, $g_1 = -21\,724\,200$, $g_2 = -19\,493\,200$, $\mu_1 = 0.532\,535$, $\mu_2 = 0$, $\mu_3 = -564.478$, $\mu_4 = -1635.46$, and $\mu^* = 28.5082$. Again we have $h > 0$ and $\mu^* > \mu_1$, which leads us to the existence of unstable hexagons H_0 [Fig. 4(b)], therefore the stable solution of ρ will not exist throughout a wide range of D. At lower diffusion ($D = 0.001$), a mixture of regular and distorted hexagons exists [see Fig. 5(d), in particular the zoomed-in view where regular hexagons are marked by the dashed white line] which is similar to Fig. 5(a). With an increase of D, we get more distorted hexagons in our considered domain [Fig. 5(e)]. A further increase in the diffusion coefficient leads most of the neurons towards the

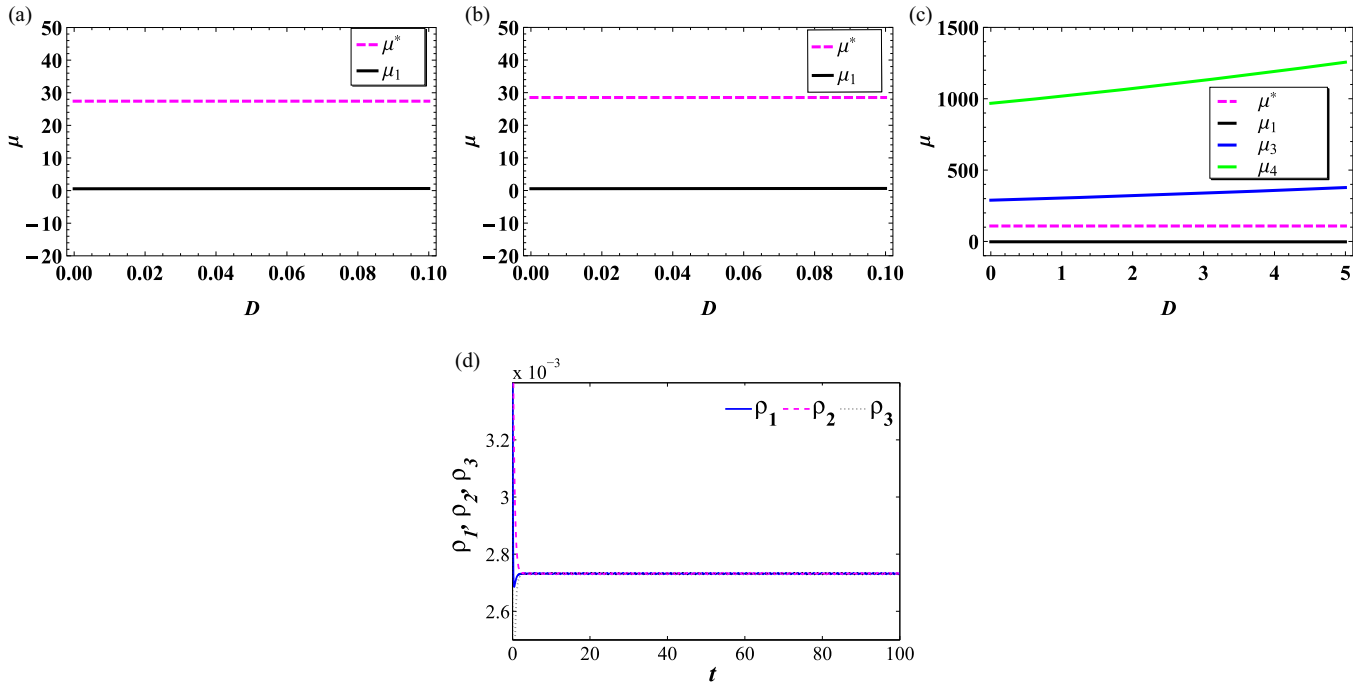

FIG. 4. Characterization of patterns of the diffusively coupled 2D ML model: boundaries of the emergence of various structures (hexagons and stripes) for (a) $I = 0.052$, (b) $I = 0.054$, and (c) $I = 0.2$. The dashed magenta line indicates the values of μ at (a) $I = 0.052$ ($\mu^* = 27.4153$), (b) $I = 0.054$ ($\mu^* = 28.508$), and (c) $I = 0.2$ ($\mu^* = 108.2896$). The thick black line indicates the condition for the existence of hexagons whereas the thick blue and green lines indicate the boundary of the stability of stripes and H_π hexagons, respectively. (d) Time integration of Eq. (24) for $I = 0.2$.

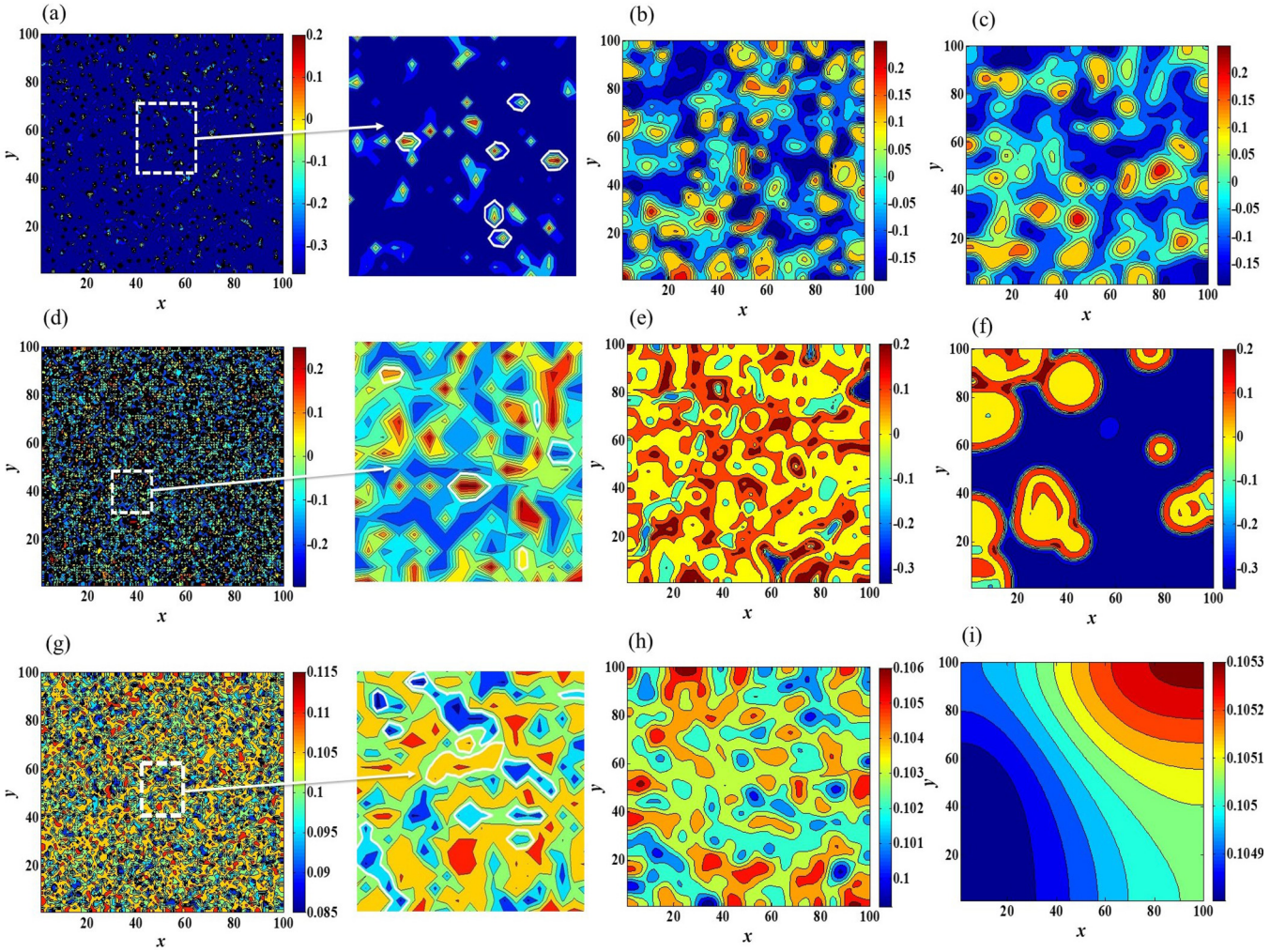

FIG. 5. Pattern formation in the 2D ML cable with 2D diffusion for (a)–(c) $I = 0.052$, (d)–(f) $I = 0.054$, and (g)–(i) $I = 0.2$ and diffusion coefficients (a), (d), and (g) $D = 0.001$; (b), (e), and (h) $D = 0.05$; (c) and (f) $D = 0.09$; and (i) $D = 5$,.

steady state of the system and only a few distorted hexagons exist [see Fig. 5(f)].

For $I = 0.2$ and $D = 0.001$, we find that $h = -14\,804.8$, $g_1 = 5\,456\,040$, $g_2 = 7\,235\,640$, $\mu_1 = -2.7498$, $\mu_2 = 0$, $\mu_3 = 377.603$, $\mu_4 = 1255.97$, and $\mu^* = 108.2896$. Here $h < 0$ and $\mu^* < \mu_4$ signify the existence of stable H_π hexagons. Also, the positivity of g_1 predicts the existence of a striped pattern. However, the inequality condition $\mu^* < \mu_3$ makes the existing stripes unstable. The variations of $\mu_{1,3,4}$ and μ^* as a function of D are shown in Fig. 4(c). As we have analytically calculated that a stable H_π exists in this parameter space, we further validate it by solving Eq. (24). The time-independent stable numerical values $\rho_{1,2,3} = 0.002\,732$ at $D = 0.001$ are shown in Fig. 4(d). Interestingly, the values of $\rho_{1,2,3}$ are properly fitted with the analytical values of ρ mentioned in (iii), the condition for the existence of hexagons. In the presence of an unstable stripe at $D = 0.001$, we get a mixture of regular and irregular hexagons [see Fig. 5(g)]. As we increase $D = 0.05$, some distorted hexagons and a small irregular stripe exist [Fig. 5(h)]. At a high value of the diffusion coefficient ($D = 5$), there is an unstable stripe leading to the homogeneous structure as the amplitude values are not significantly different in the 2D spatial domain [see Fig. 5(i)]. For $I = 0.2$ we are not getting clear hexagons because unstable stripes exist throughout the regime which break the hexagons. Also the uncoupled system is strongly in a steady (quiescence) state, therefore the amplitude is extremely small, which is reflected in the diffusion patterns.

Note that at $I = 0.052$ and $D = 0.001$, the neurons with high-amplitude oscillations (i.e., generating action potentials) are distributed in a scattered way. In the spatial domain, the neighboring nodes try to fire together or set themselves in the steady states, although neither the synchronous firing nor synchronous steady states dominate in the spatial domain. If we increase the diffusive coupling to $D = 0.05$, hexagonlike patterns (shown in red or yellow) become broader in size, suggesting that small groups of nodes are firing asynchronously, whereas inside the blue domain the neighboring nodes stay below the subthreshold oscillations. With a further increase of diffusion strength $D = 0.09$, the neurons in the spatial domain form distinct clusters (shown in red) of firing surrounded by a large subthreshold population, which will finally lead us to a homogeneous state for higher diffusion or for a long time evaluation. At $I = 0.054$ and $D = 0.001$, the network

shows the same type of feature as before. However, with an increase of diffusion to $D = 0.05$, most of the neurons divide into two domains: One group generates firing and the other shows subthreshold oscillations. With a further increase of diffusion to $D = 0.09$, most of the neurons synchronize to the quiescent state. At $I = 0.2$ for intermediate diffusion, a stable hexagonal pattern exists in which a large number of nodes fires together, although the amplitudes of the oscillatory nodes are significantly small. The domain becomes equipotential at $D = 5$, where all the neurons show synchronized steady states [see Fig. 5(i)].

The diffusively coupled 2D ML oscillator is solved using a finite-difference scheme. We discretize the space and time by taking the system as $N \times N$ with $N = 100$ and step sizes are $\Delta x = \Delta y = \Delta = 0.25$ and $\Delta t = 0.0001$ for the spatial mesh and time-integration step size, respectively. The spatial derivative is approximated as $\frac{\partial^2 u}{\partial x^2} + \frac{\partial^2 u}{\partial y^2} \rightarrow \frac{1}{\Delta^2}(u_{i-1,j} + u_{i+1,j} + u_{i,j-1} + u_{i,j+1} - 4u_{i,j})$. Note that there are no significant changes in the stability if we vary the size of the mesh grid. The spatiotemporal behavior is investigated in the context of a highly nonlinear and coupled reaction-diffusion system where the diffusive coupling indicates the synaptic coupling between the individual neurons [12] while being solved by a finite-difference scheme.

V. THE 1D CABLE OF THE 3D OSCILLATORY ML MODEL

An improved version of the 3D ML model is a slow-fast system where the slow variable is the current injected into the system [21,22]. The system variables are U, the membrane potential of the cell; V, the activation variable of K^+ ion channels; and W, the external injected current. We write the diffusion dynamics using the PDEs

$$\frac{\partial U}{\partial t} = -0.5 g_{\mathrm{Ca}}(U-1)\left[1 + \tanh\left(\frac{U - V_1}{V_2}\right)\right] - g_{\mathrm{K}} V \times (U - V_{\mathrm{K}}) - g_L(U - V_L) + W + D_1 \nabla^2 U, \quad (25)$$

$$\frac{\partial V}{\partial t} = \phi \cosh\left(\frac{U - V_3}{2V_4}\right) \times \left\{0.5\left[1 + \tanh\left(\frac{U - V_3}{V_4}\right) - V\right]\right\}, \quad (26)$$

$$\frac{\partial W}{\partial t} = -\mu(V_0 + U). \quad (27)$$

The zero-flux boundary conditions are considered for modeling the dynamical behavior of the spatially bounded ML system [17,18,41]. The nonzero equilibrium point is not locally asymptotically stable for the parameter values [21] $g_{\mathrm{Ca}} = 1.2$, $V_1 = -0.01$, $V_2 = 0.15$, $g_{\mathrm{K}} = 2$, $V_{\mathrm{K}} = -0.7$, $g_L = 0.5$, $V_L = -0.5$, $\phi = 1/3$, $V_3 = 0.1$, $V_4 = 0.05$, $V_0 = 0.2$, and $\mu = 0.005$. The ML system (25)–(27) presents a square wave bursting pattern [21] for these parameter values in the absence of diffusion. We consider a finite length of excitable cable and the time step is $\delta t = 0.01$ in the numerical treatment. The improved 3D ML model shows irregular bursting with the influence of diffusion. The system shows an irregular spike at low diffusion ($D = 0.026$) [Fig. 6(a)], which eventually leads to a nonhomogeneous irregular pattern [Fig. 6(d)].

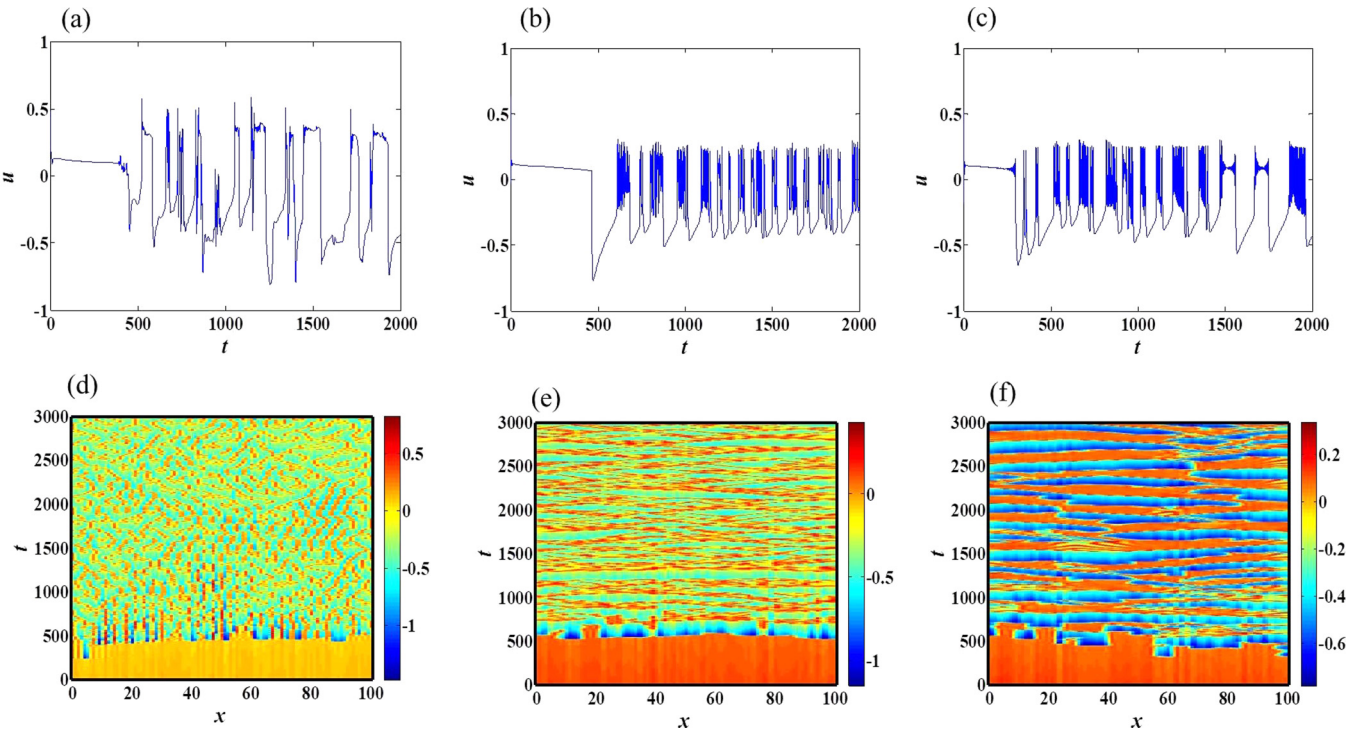

FIG. 6. Time series of the end oscillator and spatial plot of the improved 3D ML cable with 1D diffusion. The diffusion coefficients D are (a) and (d) $D = 0.026$, (b) and (e) $D = 0.4$, and (c) and (f) $D = 0.7$.

The twisted red lines in Fig. 6(d) show the high amplitude of spikes. At higher diffusion ($D = 0.4$), the system shows irregular bursting and we get a more complex pattern [see Fig. 6(b)]. The red horizontal stripes show the weakly synchronized oscillations in the system [see Fig. 6(e)]. Again at $D = 0.7$, the system shows bursting [see Fig. 6(c)] and a wavelike spatiotemporal pattern (the nodes appear correlated to each other) is generated and is shown in Fig. 6(e).

VI. CONCLUSION

In this paper a biophysically motivated 2D excitable ML model and its modification as a fast-slow 3D ML model are considered based on their neurocomputational activities. The model plays a major role in signal processing and temporal coding. By allowing diffusion in the conventional 2D ML model, we have shown several types of dynamical behavior. Interestingly, the 2D uncoupled model produces phasic and tonic spiking for a specific parameter set [21] and the system reaches a quiescent state for a higher external current stimulus. The diffusive coupling changes the collective behavior of the excitable cables and it dominates over the deterministic system. For instance, the entire 1D excitable cable (which is in the phasic spiking state or bistable regime) produces regular or irregular bursting dynamics for intermediate diffusion. We have explored the impact of 2D diffusion, which shows complex and diverse patterns including a hexagon-like structure to stripe or stationary states. In this paper the stability of corresponding patterns was thoroughly analyzed and determined using amplitude equations. We further extended our work in the 3D modified ML model setting the parameter in the periodic bursting regime. Interestingly, a 1D diffusion can create irregular bursting in the spatial domain.

We extensively demonstrated the spatial dynamical behavior of the excitable systems and explored different dynamical and collective features. The emerging properties may have particular relevance in the synchronized activities of a population of neurons particularly for neurological diseases. Analyzing pattern formation will also be helpful for the properties of the neural network [42]. We can apply the results into many areas such as associative memory, pattern recognition, and signal processing and optimization. This type of reaction-diffusion system provides ideas for future works on how chemical substances influence the dynamics of neuronal networks. For instance, the determining factors of seizurelike activities and different bursting patterns [43] can be revealed through our work. The study will also allow us to understand complex brain functions (such as brain working memory). Zero-flux boundary conditions show that the membranes are impermeable for ions [12]. Further, the method can be generalized to the exploration of the reaction-diffusion equation and different neuroscience-related topics [42,44,45]. The spatiotemporal regimes studied in this paper and their relation to neurocomputational behavior can be further investigated in future experiments. This work helps us in understanding the nonlinear dynamics and spatial behavior of an excitable cable.

ACKNOWLEDGMENTS

This work was supported by the University Grants Commission, Government of India, under a NET-JRF scholarship to S.K.S. and by Council of Scientific and Industrial Research, Government of India, under Grant No. 25(0277)/17/EMR-II) to R.K.U. C.H. was supported by DST-INSPIRE Faculty Grant No. IFA17-PH193. P.K. acknowledges support from DST, India, under DST-INSPIRE Grant No. IF140880. We would also like to thank the anonymous referee for valuable suggestions and comments.

APPENDIX A: ANALYSIS OF AMPLITUDE STABILITY

We discuss the stability of the above three sets of fixed points. In the case of striped patterns, we perturb the fixed point $(\rho_0, 0, 0)$ to study the stability of the stationary solution (24), where $\rho_0 = \sqrt{\mu/g_1}$. Setting $\rho_i = \rho_0 + \Delta\rho_i$, $i = 1, 2, 3$, the linearization of Eq. (24) can be written as

$$\frac{\partial \rho}{\partial t} = L_A \rho, \tag{A1}$$

where

$$L_A = \begin{pmatrix} \mu - 3g_1\rho_0^2 & 0 & 0 \\ 0 & \mu - g_2\rho_0^2 & h\rho_0 \\ 0 & h\rho_0 & \mu - g_2\rho_0^2 \end{pmatrix},$$

$$\rho = \begin{pmatrix} \Delta\rho_1 \\ \Delta\rho_2 \\ \Delta\rho_3 \end{pmatrix}.$$

The characteristic equation of L_A can be written as

$$\lambda^3 + R_1\lambda^2 + R_2\lambda + R_3 = 0, \tag{A2}$$

where

$$R_1 = (3g_1 + 2g_2)\rho_0^2 - 3\mu,$$

$$R_2 = \left(g_2^2 + 6g_2g_1\right)\rho_0^4 - (4\mu g_2 + h^2 + 6\mu g_1)\rho_0^2 + 3\mu^2,$$

$$R_3 = 3g_1g_2^2\rho_0^6 - (3g_1h^2 + \mu g_2^2 + 6\mu g_1g_2)\rho_0^4 - (2\mu^2 g_2 + 3g_1\mu^2 + \mu h^2)\rho_0^2 - \mu^3.$$

The eigenvalues of the characteristic equation (A2) can be obtained as

$$\lambda_1 = -2\mu,$$

$$\lambda_2 = \mu\left(1 - \frac{g_2}{g_1}\right) + h\sqrt{\frac{\mu}{g_1}},$$

$$\lambda_3 = \mu\left(1 - \frac{g_2}{g_1}\right) - h\sqrt{\frac{\mu}{g_1}}.$$

The system will be stable if all the eigenvalues are negative. These three eigenvalues are negative if the conditions $\mu > 0$, $\frac{g_2}{g_1} > 1$, and $\mu > \mu_3 = \frac{h^2 g_1}{(g_2 - g_1)^2}$ hold. Next we consider the case of hexagon. We perturb the fixed point (ρ_0, ρ_0, ρ_0) to study the stability of the stationary solution, i.e., Eq. (24), $\rho_i = \rho_0 + \Delta\rho_i$ $(i = 1, 2, 3)$, where $\rho_0 = \frac{|h| \pm \sqrt{h^2 + 4(g_1 + 2g_2)\mu}}{2(g_1 + 2g_2)}$. Equation (24) can be linearized as

$$\frac{\partial \rho}{\partial t} = L_B \rho, \tag{A3}$$

where

$$L_B = \begin{pmatrix} \mu - 3g_1\rho_0^2 - 2g_2\rho_0^2 & h\rho_0 - 2g_2\rho_0^2 & h\rho_0 - 2g_2\rho_0^2 \\ h\rho_0 - 2g_2\rho_0^2 & \mu - 3g_1\rho_0^2 - 2g_2\rho_0^2 & h\rho_0 - 2g_2\rho_0^2 \\ h\rho_0 - 2g_2\rho_0^2 & h\rho_0 - 2g_2\rho_0^2 & \mu - 3g_1\rho_0^2 - 2g_2\rho_0^2 \end{pmatrix},$$

$$\rho = \begin{pmatrix} \Delta\rho_1 \\ \Delta\rho_2 \\ \Delta\rho_3 \end{pmatrix}.$$

The characteristic equation of L_B can be written as

$$\lambda^3 + S_1\lambda^2 + S_2\lambda + S_3 = 0, \tag{A4}$$

where

$$S_1 = (9g_1 + 6g_2)\rho_0^2 - 3\mu,$$
$$S_2 = \left(27g_1^2 + 36g_2g_1\right)\rho_0^4 + 12g_2h\rho_0^3 - (18\mu g_1 + 3h^2 + 12\mu g_2)\rho_0^2 + 3\mu^2,$$
$$S_3 = \left(54g_1^2g_2 + 27g_1^3\right)\rho_0^6 + 36g_1g_2h\rho_0^5 + \left(6g_2h^2 - 36\mu g_1g_2 - 9g_1h^2 - 27\mu g_1^2\right)\rho_0^4 (2h^2 + 12\mu h g_2)\rho_0^3$$
$$+ (9\mu^2 g_1 + 6\mu^2 g_2 + 3\mu h^2)\rho_0^2 - \mu^3.$$

The characteristic equation (A4) can be solved to obtain the eigenvalues $\lambda_1 = \lambda_2 = \mu - h\rho_0 - 3g_1\rho_0^2$ and $\lambda_3 = \mu + 2h\rho_0 - 3\rho_0^2(g_1 + 2g_2)$. The system (24) has a stable solution when all the eigenvalues are negative. For $\rho_0^- = \frac{|h| - \sqrt{h^2 + 4(g_1+2g_2)\mu}}{2(g_1+2g_2)}$, λ_1 and λ_2 are always positive, so the corresponding pattern is always unstable. For $\rho_0^+ = \frac{|h| + \sqrt{h^2 + 4(g_1+2g_2)\mu}}{2(g_1+2g_2)}$, all the eigenvalues are negative if the parameter μ satisfies the condition $\mu < \mu_4 = \frac{2g_1+g_2}{(g_2-g_1)^2}h^2$.

APPENDIX B: COMPUTATIONS OF THE PARAMETERS

The following are the coefficients of Eqs. (7) and (8):

$$a_1 = -g_L - 0.5g_{\mathrm{Ca}} + \frac{0.5g_{\mathrm{Ca}}}{V_2}\left[V_1 - \frac{{V_1}^3}{3V_2^2} + V_{\mathrm{Ca}} - \frac{V_{\mathrm{Ca}}V_1^2}{V_2^2}\right],$$
$$a_2 = g_{\mathrm{K}}V_{\mathrm{K}}, \quad a_3 = \frac{0.5g_{\mathrm{Ca}}}{V_2}\left[-1 + \frac{V_1^2}{V_2^2} + \frac{V_{\mathrm{Ca}}V_1}{V_2^2}\right],$$
$$a_4 = -g_{\mathrm{K}},$$
$$a_5 = \frac{-0.5g_{\mathrm{Ca}}}{V_2^3}\left[V_1 + \frac{V_{\mathrm{Ca}}}{3}\right],$$
$$a_6 = V_Lg_L + 0.5V_{\mathrm{Ca}}g_{\mathrm{Ca}} - \frac{0.5V_{\mathrm{Ca}}g_{\mathrm{Ca}}V_1}{V_2}\left[1 - \frac{V_1^2}{3V_2^2}\right],$$
$$b_1 = \frac{0.5}{3V_4}\left[1 - \frac{5V_3^2}{8V_4^2} - \frac{V_3}{4V_4} - \frac{5V_3^4}{24V_4^4}\right],$$
$$b_2 = -\frac{1}{3} - \frac{V_3^2}{24V_4^2},$$
$$b_3 = \frac{0.5}{3V_4^2}\left[\frac{V_3}{V_4} + \frac{1}{8} - \frac{3V_3}{8V_4} + \frac{5V_3^3}{12V_4^3}\right],$$
$$b_4 = \frac{V_3}{12V_4^2},$$
$$b_5 = \frac{-2.5}{72V_4^3} - \frac{5V_3^2}{72V_4^5}, \quad b_6 = \frac{-1}{24V_4^2},$$
$$b_7 = \frac{0.5}{3}\left[1 - \frac{V_3}{V_4} - \frac{5V_3^3}{24V_4^3} + \frac{V_3^2}{8V_4^2} + \frac{V_3^5}{24V_4^5}\right].$$

12 626 The following are expressions of some parameters used in the multiple-scale expansion method:

$$\begin{pmatrix} P_0 \\ Q_0 \end{pmatrix} = \begin{pmatrix} z_{p_0} \\ z_{q_0} \end{pmatrix}(|W_1|^2 + |W_2|^2 + |W_3|^2),$$

$$P_j = fQ_j, \quad \begin{pmatrix} P_{jj} \\ Q_{jj} \end{pmatrix} = \begin{pmatrix} z_{p_1} \\ z_{q_1} \end{pmatrix} W_j^2, \quad \begin{pmatrix} P_{jk} \\ Q_{jk} \end{pmatrix} = \begin{pmatrix} z_{p_2} \\ z_{q_2} \end{pmatrix} W_j \bar{W}_k,$$

$$\tau_0 = \frac{f+g}{I_T[fm_{11}+m_{12}+g(fm_{21}+m_{22})]},$$

$$h = \frac{\mathbf{H}}{I_T[fm_{11}+m_{12}+g(fm_{21}+m_{22})]},$$

$$g_1 = \frac{G_1}{I_T[fm_{11}+m_{12}+g(fm_{21}+m_{22})]},$$

$$g_2 = \frac{G_2}{I_T[fm_{11}+m_{12}+g(fm_{21}+m_{22})]},$$

$$\mathbf{H} = 2(l_1 + gl_2),$$

$$l_1 = f^2(a_3 + 3a_5u^*) + fa_4, \quad l_2 = f^2(b_3 + 3b_5u^* + b_6v^*) + f(b_4 + 2b_6u^*),$$

$$k_T^2 = \frac{\Delta_0^T}{Da_{22}^T}, \quad \Delta_0^T = a_{11}^T a_{22}^T - a_{12}^T a_{21}^T,$$

$$h_2 = \left[(a_3 + 3a_5u^*)p_1^2 + a_4p_1q_1(b_3 + 3b_5u^* + b_6v^*)p_1^2 + (b_4 + 2b_6u^*)p_1q_1\right],$$

$$h_3 = \left[2(a_3 + 3a_5u^*)p_1p_2 + a_4(p_1q_2 + p_2q_1) + a_5p_1^3 2(b_3 + 3b_5u^* + b_6v^*)p_1p_2 + (b_4 + 2b_6u^*)(p_1q_2 + p_2q_1)\right.$$
$$\left. + b_5p_1^3 + b_6p_1^2q_1\right],$$

$$\begin{pmatrix} z_{p_0} \\ z_{q_0} \end{pmatrix} = \frac{-2}{\Delta_0^T}\begin{pmatrix} a_{22}^T l_1 - a_{12}^T l_2 \\ a_{11}^T l_2 - a_{21}^T l_1 \end{pmatrix},$$

$$\begin{pmatrix} z_{p_1} \\ z_{q_1} \end{pmatrix} = \frac{-1}{(a_{11}^T - 4Dk_T^{2T})a_{22}^T - a_{12}^T a_{21}^T}\begin{pmatrix} a_{22}^T l_1 - a_{12}^T l_2 \\ (a_{11}^T - 4Dk_T^{2T})l_2 - a_{21}^T l_1 \end{pmatrix},$$

$$\alpha_1 = (a_3 + 3a_5u^*), \quad \beta_1 = a_4, \quad \gamma_1 = a_5, \quad \delta_2 = b_6,$$

$$\begin{pmatrix} z_{p_2} \\ z_{q_2} \end{pmatrix} = \frac{-2}{(a_{11}^T - 3Dk_T^{2T})a_{22}^T - a_{12}^T a_{21}^T}\begin{pmatrix} a_{22}^T l_1 - a_{12}^T l_2 \\ (a_{11}^T - 3Dk_T^{2T})l_2 - a_{21}^T l_1 \end{pmatrix},$$

$$\alpha_2 = (b_3 + 3b_5u^* + b_6v^*), \quad \beta_2 = (b_4 + 2b_6u^*), \quad \gamma_2 = b_5,$$

$$m_{11} = \{-[g_{\mathrm{Ca}}(1/\{V_2\cosh[(V_1-u^*)/V_2]^2\} - \{\tanh[(V_1-u^*)/V_2]^2 - 1\}/V_2$$
$$+ \{2\sinh[(V_1-u^*)/V_2](u^*-1)\}/\{V_2^2\cosh[(V_1-u^*)/V_2]^3\})/2][g_L + g_{\mathrm{K}}v^* - (g_{\mathrm{Ca}}\{\tanh[(V_1-u^*)/V_2] - 1\})/2$$
$$+ (g_{\mathrm{Ca}}\{\tanh[(V_1-u^*)/V_2]^2 - 1\}(V_{\mathrm{Ca}} - u^*))/2V_2]^{-1} - 1/(u^* - V_k),$$

$$m_{12} = (-g_{\mathrm{K}})/[g_L + g_{\mathrm{K}}v^* - (g_{\mathrm{Ca}}\{\tanh[(V_1-u^*)/V_2] - 1\})/2 + (g_{\mathrm{Ca}}\{\tanh[(V_1-u^*)/V_2]^2 - 1\}(V_{\mathrm{Ca}} - u^*))/2V_2],$$

$$m_{21} = [(\phi\sinh[(V_3-u^*)/2V_4]\{\tanh[(V_3-u^*)/V_4]^2 - 1\})/4V_4^2 - (\phi\cosh[(V_3-u^*)/2V_4]\{v^*$$
$$+ \tanh[(V_3-u^*)/V_4]/2 - 0.5\})/4V_4^2 - \{\phi\sinh[(V_3-u^*)/2V_4]\}/\{4V_4^2\cosh[(V_3-u^*)/V_4]^2\}$$
$$+ \{\phi\cosh[(V_3-u^*)/2V_4]\sinh[(V_3-u^*)/V_4]\}/\{V_4^2\cosh[(V_3-u^*)/V_4]^3\}]/[g_L + g_{\mathrm{K}}v^*$$
$$- (g_{\mathrm{Ca}}\{\tanh[(V_1-u^*)/V_2] - 1\})/2 + (g_{\mathrm{Ca}}\{\tanh[(V_1-u^*)/V_2]^2 - 1\}(V_{\mathrm{Ca}} - u^*))/2V_2]$$
$$+ \phi\sinh[(V_3-u^*)/2V_4]/2V_4g_{\mathrm{K}}(u^* - V_{\mathrm{K}}),$$

$$m_{22} = \{\phi\sinh[(V_3-u^*)/2V_4]\}/2V_4[g_L + g_{\mathrm{K}}v^* - (g_{\mathrm{Ca}}\{\tanh[(V_1-u^*)/V_2] - 1\})/2$$
$$+ (g_{\mathrm{Ca}}\{\tanh[(V_1-u^*)/V_2]^2 - 1\}(V_{\mathrm{Ca}} - u^*))/2V_2],$$

$$-G_1 = \left[(2\alpha_1 f + \beta_1)(z_{p_0} + z_{p_1}) + \beta_1 f(z_{q_0} + z_{q_1}) + 3\gamma_1 f^3\right] + g\left[(2\alpha_2 f + \beta_2)(z_{p_0} + z_{p_1}) + \beta_2 f(z_{q_0} + z_{q_1}) + 3\delta_2 f^2 + 3\gamma_2 f^3\right],$$

$$-G_2 = \left[(2\alpha_1 f + \beta_1)(z_{p_2} + z_{p_0}) + \beta_1 f(z_{q_2} + z_{q_0}) + 6\gamma_1 f^3\right] + g\left[(2\alpha_2 f + \beta_2)(z_{p_2} + z_{p_0}) + \beta_2 f(z_{q_2} + z_{q_0}) + 6\gamma_2 f^3 + 6\delta_2 f^2\right].$$

Q
[1] A. Turing, Philos. Trans. R. Soc. London **237**, 37 (1952).
[2] L. A. Segel and J. L. Jackson, J. Theor. Biol. **37**, 545 (1972); M. Banerjee and S. Petrovskii, Theor. Ecol. **4**, 37 (2011).
13
[3] S. Yuan, C. Xu, and T. Zhang, Chaos **23**, 033102 (2013).
[4] T. Zhang, Y. Xing, H. Zang, and M. Han, Nonlinear Dyn. **78**, 265 (2014).
[5] Q. Ouyang and H. L. Swinney, Chaos **1**, 411 (1991).
[6] S. Sick, S. Reinker, J. Timmer, and T. Schlake, Science **314**, 1447 (2006).
[7] R. A. Barrio, R. E. Baker, B. Vaughan, Jr., K. Tribuzy, M. R. de Carvalho, R. Bassanezi, and P. K. Maini, Phys. Rev. E **79**, 031908 (2009).
[8] S. Kondo, Genes Cells **7**, 535 (2002).
Q
[9] A. L. Slusarczyk and R. Weiss, Sci. Signal **5**, pe16 (2012).
[10] S. Kondo and T. Miura, Science **329**, 1616 (2010).
[11] T. Jr. Bansagi, V. K. Vanag, and I. R. Epstein, Science **331**, 1309 (2011).
[12] S. R. Meier, J. L. Lancaster, and J. M. Starobin, PLoS One **10**, e0122401 (2015).
[13] M. Bär and M. Eiswirth, Phys. Rev. E **48**, R1635(R) (1993).
[14] M. Kuznetsov, A. Kolobov, and A. Polezhaev, Phys. Rev. E **95**, 052208 (2017).
[15] G. Gambino, M. C. Lombardo, G. Rubino, and M. Sammartino,
14
Ric. Mat. **65**, 449 (2018).
[16] S. Raghavachari and J. A. Glazier, Phys. Rev. Lett. **82**, 2991 (1999).
[17] B. Ambrosio and M. A. Aziz-Alaoui, Comput. Math. Appl. **64**, 934 (2012).
[18] B. Ermentrout and M. Lewis, Bull. Math. Biol. **59**, 533 (1997).
[19] J. J. Tyson, in *Cell to Cell Signalling: From Experiments to Theoretical Models*, edited by A. Goldbeter (Academic, New
15
York, 1989), pp. 521–537.
[20] C. Morris and H. Lecar, Biophys. J. **35**, 193 (1981).
[21] E. M. Izhikevich, Int. J. Bifurcat. Chaos **10**, 1171 (2000).
[22] E. M. Izhikevich, IEEE Trans. Neural Netw. **15**, 1063 (2004).
[23] S. Brunak and B. Lautrup, *Neural Networks* (World Scientific, Singapore, 1990).
[24] R. A. Stefanescu and V. K. Jirsa, PLoS Comput. Biol. **4**, e1000219 (2008).
[25] F. M. M. Kakmeni, E. M. Inack, and E. M. Yamakou, Phys. Rev. E **89**, 052919 (2014).
[26] Z. P. Kilpatrick and P. C. Bressloff, Physica D **239**, 547 (2010).
[27] D. D. Clarke and L. Sokoloff, in *Basic Neurochemistry: Molecular, Cellular and Medical Aspects*, edited by G. J. Siegel, B. W. Agranoff, R. W. Albers, S. K. Fisher, and M. D. Uhler (Lippincott-Raven, Philadelphia, 1999).
16
[28] S. E. Folias and P. Bressloff, SIAM J. Appl. Math. **65**, 2067 (2005).
[29] G. Q. Sun, C. H. Wang, and Z. Y. Wu, Nonlinear Dyn. **88**, 1385 (2017).
[30] H. Zhao, X. Huang, and X. Zhang, Nonlinear Dyn. **76**, 115 (2014).
[31] M. C. Cross and P. C. Hohenberg, Rev. Mod. Phys. **65**, 851 (1993).
[32] A. C. Newell and J. A. Whitehead, J. Fluid Mech. **38**, 279 (1969).
[33] L. A. Segel, J. Fluid Mech. **38**, 203 (1969).
[34] T. Tateno and K. Pakdaman, Chaos **14**, 511 (2004).
[35] A. Koseska, E. Volkov, and J. Kurths, Phys. Rev. Lett. **111**, 024103 (2013); C. R. Hens, O. I. Olusola, P. Pal, and S. K. Dana, Phys. Rev. E **88**, 034902 (2013); T. Banerjee and D. Ghosh, **89**, 062902 (2014).
[36] M. Perez-Armandriz, M. C. Roy, D. C. Spray, and M. V. L. Bennet, Biophys. J. **59**, 76 (1991).
[37] C. Hens, P. Pal, and S. K. Dana, Phys. Rev. E **92**, 022915 (2015).
[38] M. Ipsen, F. Hynne, and P. G. Sørensen, Physica D **136**, 66 (2000).
[39] M. Ipsen, L. Kramer, and P. G. Sørensen, Phys. Rep. **337**, 193 (2000).
[40] A. De Wit, Adv. Chem. Phys. **109**, 435 (1999).
Q
[41] B. Ambrosio and J. P. Françoise, Philos. Trans. R. Soc. A **367**, 4863 (2009).
[42] B. Ermentrout, Rep. Prog. Phys. **61**, 353 (1998).
[43] N. G. Rambidi, T. O. Kuular, and E. E. Makhaeva, Adv. Funct. Mater. **8**, 163 (1998).
Q
[44] C. A. Del Negro, C. F. Hsiao, S. H. Chandler, and A. Garfinkel, Biophys. J. **75**, 174 (1998).
[45] O. V. Aslanidi and O. A. Mornev, J. Biol. Phys. **25**, 149 (1999).